Journal of Alloys and Compounds 916 (2022) 165438

Contents lists available at ScienceDirect

Journal of Alloys and Compounds

journal homepage: www.elsevier.com/locate/jalcom

Research Article

Iron (II) fluoride cathode material derived from MIL-88A

Vera V. Butova[a,*], Abdelaziz M. Aboraia[a,b], Victor V. Shapovalov[a], Narek A. Dzhangiryan[c], Elizaveta D. Papkovskaya[c], Oleg I. Ilin[d], Stanislav P. Kubrin[e], Alexander A. Guda[a], Alexander V. Soldatov[a]

[a] The Smart Materials Research Institute, Southern Federal University, Sladkova 178/24, 344090 Rostov-on-Don, Russian Federation
[b] Department of Physics, Faculty of Science, Al-Azhar University, Assiut 71542, Egypt
[c] Chemistry Faculty, Southern Federal University, 7 Zorge Street, Rostov-on-Don, Russian Federation
[d] Institute of Nanotechnologies, Electronics and Equipment Engineering, Southern Federal University, Shevchenko 2, 347922 Taganrog, Russian Federation
[e] Research Institute of Physics, Southern Federal University, 194, Stachki avenue, Rostov-on-Don 344090, Russian Federation

ARTICLE INFO

Article history:
Received 15 October 2021
Received in revised form 8 April 2022
Accepted 12 May 2022
Available online 16 May 2022

Keywords:
MOF
Iron fumarate
FeF_2
Conversion cathode
XANES
Electron diffraction

ABSTRACT

We report an eco-friendly, simple, and scalable method of FeF_2 cathode production. MIL-88A was synthesized in a water medium without any additives. It was used as a source of iron (3 +) ions during pyrolysis. The porous structure of such a sacrificial agent allowed us to incorporate poly-vinylidene fluoride molecules as a guest component into a host MIL-88A framework. Pyrolysis in Ar-flow results in two simultaneous processes: reducing Fe^{3+} into Fe^{2+} and forming porous carbon shells for FeF_2 nanoparticles. Applying complex analysis of high-resolution TEM images, porosity measurements, and XANES spectroscopy, we have revealed that obtained iron fluoride is composed of nanoparticles with elongated and hexagonal shapes. Both iron fluorides were attributed to tetragonal FeF_2 structure type, contained only Fe^{2+} ions, and were covered with porous carbon shells. The obtained material was used as a cathode for a lithium-ion battery and showed good stability and a high capacity of 425–330 mA h/g. The proposed water-based synthesis of MIL-88A as a precursor in combination with mild pyrolysis conditions and good electrochemical performance make this material promising for cathode application.

1. Introduction

Lithium-ion batteries (LIB) are widely used in portable devices as a rechargeable power supply. Commercial LIBs usually contain such cathodes as $LiCoO_2$, $LiFePO_4$, and others. These materials could be attributed to the intercalation type of cathodes. Lithium ions insert into the host matrix via available pathways (tunnels or planes) during the discharge step. Although intercalation cathodes possess good reversibility, their capacity is limited by the number of available Li-sites. Conversion cathodes are considered a possible alternative to intercalation ones [1,2]. They exhibit a large specific capacity due to conversion reactions with more than one permitted electron transfer. During a lithiation/de-lithiation process, the chemical interaction of conversion electrodes with lithium ions leads to a change of cathode crystal structure with the breaking and recombining of chemical bonds [2]. Oxides [3–5], hydrides [6–8], sulfides [9,10], nitrides [11–13], and fluorides [14,15] of transition metals renew interest as high-capacity conversion electrodes.

Iron fluorides (FeF_2 and FeF_3) have been actively pursued due to intermediate operation voltages and high theoretical specific and volumetric capacities. For instance, FeF_2 reacts with two Li-ions at around 2.66 V, with a theoretical capacity of about 571 mA h/g, which results in a theoretical energy density of 1518 W h/kg [16–21]. The mechanism of this reaction was reported by Wang et al. [20,22]. Mobile fluoride ions migrated out of FeF_2 particles and interacted with lithium ions producing lithium fluoride. The remaining Fe^{2+} ions, after reduction, formed a new phase of metallic nanoparticles inside of LiF matrix.

Pure FeF_2 is an electrical insulator. It also exhibits slow diffusion of lithium ions after the initial insertion due to strong phase separation between LiF and Fe, characterized by both high resistance and high capacitance (due to the high interfacial surface). It results in a large overpotential and a strong polarization, observed as a large voltage hysteresis among lithiation/de-lithiation processes [23]. Consequently, stable nanocrystallite iron fluoride in the conductive carbon matrix is required to provide the electronic path to enhance the kinetics of a reaction and shield the volume changes [24,25].

* Corresponding author.
E-mail address: vbutova@sfedu.ru (V.V. Butova).

https://doi.org/10.1016/j.jallcom.2022.165438
0925-8388/

Coating of iron fluoride by carbon increases the surface area and reduces the ion diffusion length overcoming these problems [25–27]. The carbon layer thickness is a very crucial parameter. Zhang et al. prepared FeF_2 with carbon nanorods utilizing a polyvinylidene fluoride and ferrocene mix. However, the carbon layer was thick, which resulted in limited lithium diffusion. Besides, the carbon shells were filled by FeF_2 cores. It led to insufficient buffer space for FeF_2 volume expansion upon discharge reactions [28]. Therefore, the electrochemical performance was poor. Xiao et al. reported the synthesis of FeF_2 from iron(II) trifluoroacetate [29]. Firstly, the precursor was obtained via a solvothermal route from iron chloride and trifluoroacetic acid. Then, it was decomposed in the high-boiling solvent under argon protection at 310 °C. Synthesized material exhibited near theoretical capacity and high cycling stability in an ionic liquid electrolyte. Earlier, a solid polymer electrolyte was proposed for constructing FeF_2 electrodes. Pyrolysis of non-woven carbon nanotube fabric impregnated with $FeSiF_6$ resulted in long-cycle stability and high-capacity (> 450 mA h/g) of FeF_2 cathodes [30]. The electrochemical synthesis was also tested for the production of iron fluoride composites with carbon [31]. Fe^{2+} ions were incorporated into graphite fluoride via electrochemical interaction. The reversible capacity of synthesized material was 349 mA h/g after 20 cycles. Authors have attributed such cycling performance to the homogeneous distribution of iron fluoride nanoparticles within the carbon matrix. In a recent paper, the synthesis of dendrite-structured FeF_2 was reported [25]. Ferrocene was applied as a source of iron, while a hydrofluoric acid provided F^- ions. The solvothermal treatment with subsequent pyrolysis resulted in the formation of dendritic FeF_2 particles. The material showed a high specific capacity of 275 mA h/g within a 1.5–4 V vs Li^+/Li voltage at 100 mA/g [25].

Despite many reports focused on FeF_2 cathodes, many issues should be addressed to commercialize such materials successfully (Table S1 in SI). Firstly, the synthesis of FeF_2 often required an inert atmosphere [29] and/or non-aqueous solvents [25,28,31,32]. Additionally, carbon shell formation is often realized as a separate stage with expensive and non-stable organic precursors. Thus, the design of a new, simple, environmentally friendly synthesis route for FeF_2 cathodes with a suitable microstructure for Li-ion diffusion is still a challenge. In this sense, metal-organic frameworks (MOFs) are considered alternative precursors of both metal ions and carbon. MOFs are constructed from metallic clusters and organic molecules – linkers [33,34]. These crystalline porous materials are often used as sacrificial agents to produce metallic or metal oxide nanoparticles [35–39]. Fe-based MOFs are able to provide Fe-ions for the synthesis of iron fluorides. MIL-88B was used for such aims. This MOF is composed of Fe^{3+} ions and terephthalic acid. Two of the proposed procedures included the following stages. In the first stage, MIL-88B was decomposed with the formation of metallic iron [40] or iron oxide [32]. The iron precursor interacted with H_2SiF_6 with subsequent pyrolysis and formation of FeOF [40] or FeF_2 [32]on carbon. Cheng et al. recently proposed the synthesis of FeF_3 material via interaction of MIL-88B with NH_4F during the pyrolysis process [41]. However, MIL-88B could not be obtained in a water medium because its linker – terephthalic acid – is insoluble in water. All mentioned procedures included the synthesis of MIL-88B in DMF as the first stage.

We have chosen MIL-88A as an iron and carbon precursor in the present work. It comprises Fe^{3+} ions and fumarate linkers (SI Fig. S1) [42,43]. This MOF could be synthesized in water without any additives. In a list of reports, MIL-88A was used to obtain nanoparticles of metallic iron or its oxides [44–47]. To the best of our knowledge, MIL-88A was not used for the production of FeF_2 or other fluorides. Water-based synthesis and cheap, eco-friendly precursors make this MOF extremely attractive for application as a sacrificial agent. We also used polyvinylidene fluoride as an F^- source to provide additional carbon for composite. Finally, a relatively mild condition of pyrolysis makes the proposed technique suitable for FeF_2@carbon cathodes synthesis.

2. Experimental

Starting materials $FeCl_3{\cdot}6H_2O$, fumaric acid, poly(vinylidene fluoride) (Mw ~ 534, designated in text as PVDF), methanol were purchased from commercial suppliers and used without additional purification. We used 1 M $LiPF_6$ solution in a mixture of ethylene carbonate (EC) with dimethylecarbonate (DMC) in a ratio of 1:1 produced by Sigma for electrochemical measurements. Ultrapure deionized water was obtained from distilled one utilizing a water treatment system Simplicity-UV.

2.1. Synthesis of MIL-88A

In a typical synthesis, fumaric acid (696.4 mg, 6 mmol) was completely dissolved in 150 ml of hot water. Then the clear solution was naturally cooled to room temperature. $FeCl_3{\cdot}6H_2O$ (1621.8 mg, 6 mmol) was dissolved in 10 ml of water without heating and poured into the fumaric acid solution. Additional 10 ml of water were used to collect all $FeCl_3$ residuals and transfer them to the reaction mixture. The total volume of the resulting solution was 170 ml. It was placed into the preheated oven in the conical capped flask and held at 70 °C for 19 h. Orange precipitate was collected via centrifugation, washed twice with water and one time with methanol, and dried at 60 °C for 10 h. The yield of the product was estimated at 70%.

2.2. Carbonization

PVDF powder (326.8 mg, 0.6 mmol) was suspended in 5 ml of methanol. Dry MIL-88A precipitate (50 mg, 0.09 mmol) was added to the white suspension and stirred for 2 h at room temperature. After this, the light-orange powder was collected via centrifugation, washed with methanol, and dried at 60 °C for 10 h. Finally, the obtained mixture was calcinated in a tube oven at 450 °C for 1 h in argon flow. The black powdered product was referred to as FeF_2@C (Fig. 1).

We reproduced calcination in the airflow to trace the effect of an inert atmosphere on the phase composition of the product. The sample, after heating in the air at 450 °C for 1 h was referred to as MIL-88A-PVDF-air.

2.3. Electrochemical performance

FeF_2@C powder was mixed and mortared with 25 wt% of carbon (Timcal Super P Conductive, Alpha Aesar) and 5 wt% of PVDF binder (Sigma, 5% solution in NMP) with an additional 40 wt% (relative to the total mass of the mixture) of pure NMP added afterward to reach the viscosity required for electrode deposition. The resulting slurry was deposited onto glassy carbon disks to form electrodes (5 mm in diameter) with the FeF_2@C mass load of ~ 1.43 mg/cm [2]. Electrodes

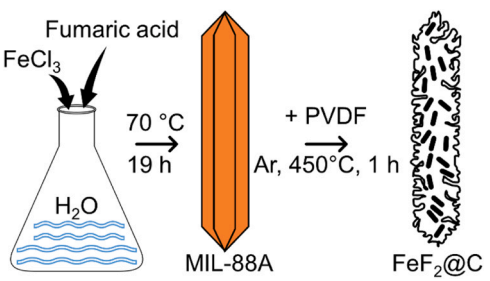

Fig. 1. Scheme of FeF_2@C synthesis.

were then dried at 80 °C in an anaerobic atmosphere for 8 h. It was used as a cathode into a Swagelok-type electrochemical cell with Li foil (G-Materials, Germany, 250 µm thickness) as an anode, 1 M $LiPF_6$ in 1:1 EC:DMC (v/v, battery grade, Sigma Aldrich) as an electrolyte, and Celgard 2600 polymer film (Celgard, USA) as a separator. The cell was galvanostatically cycled using an SP200 potentiostat/galvanostat (Biologic Instruments, France) with a current density of ~ 170 mA/g (relative to the FeF_2@C mass) between 1.3 V and 4.2 V vs Li/Li^+.

2.4. Characterization techniques

D2 PHASER diffractometer (Bruker Corporation, Germany) was utilized for X-ray powder diffraction (XRD). Profiles were collected in 2θ range 5–70° with 0.01 step (CuKα, λ = 1.5417 Å). Profile analysis was performed in Jana2006 software [48]. Transmission electron microscope FEI Tecnai G2 Spirit TWIN was used for microscopy (TEM) with accelerating voltage – 80 kV. IR spectra were recorded on a spectrometer Bruker Vertex 70 in ATR geometry (Attenuated total reflectance) from 5000 to 30 cm^{-1}. We used an MCT detector and a Bruker Platinum ATR attachment. The resolution was 1 cm^{-1} and 64 scans. Nitrogen adsorption/desorption isotherms were measured on Accelerated Surface Area and Porosimetry analyzer ASAP 2020 (Micromeritics) at − 196 °C. The specific surface area values were calculated according to the Brunauer–Emmett–Teller (BET) model. The samples were degassed at 150 °C for 12 h under a dynamic vacuum before the measurement. The thermal gravimetric analyzer (Netzsch) was applied for thermogravimetric analysis (TGA) and differential scanning calorimetry (DSC). Samples in corundum crucibles were heated with a rate of 10°/min in the airflow. Scanning electron microscope (SEM) Nova Nanolab 600 (FEI, Netherlands) was used for samples topological control. Genesis SPECTRUM spectrometer (EDAX AMETEK, USA) was used for elemental composition analysis by energy-dispersive X-ray spectroscopy (EDX). EDX spectra were obtained with 10 kV accelerating voltage and 2.4 nA electron beam current. The signal accumulation time in each point was 15 s.

X-ray absorption near edge structure (XANES) spectra of the Fe K-edge were measured using the R-XAS Looper (Rigaku, Japan) laboratory X-Ray absorption spectrometer at the Smart Materials Research Institute of Southern Federal University. All measurements were performed in transmission geometry with Ge (311) crystal as a monochromator, providing energy resolution ΔE = 1.4 eV at the energy of Fe K-edge (7112 eV). The incident beam intensity was measured by Ar-filled (300 mbar) ionization chamber, transmitted intensity – by scintillation counter with a photomultiplier tube. Acquired spectra were measured in 3 scans with subsequent averaging, normalization, and flattening using the Athena tool from the Demeter package [49].

Mossbauer spectrum was measured using MS1104Em spectrometer. The ^{57}Co in rhodium matrix was used as γ-quanta source. The spectrum was fitted with the aid of SpectrRelax software. The isomer shifts were calculated using metallic α-Fe as reference.

2.5. MIL-88A

XRD pattern of obtained MIL-88A sample is presented in Fig. 2a. Its structure could be assigned to the "open" modification of MIL-88A [50]. All peaks were fitted in hexagonal symmetry, space group *P*-62*c* (190). Lattice constants were estimated as a = 13.7420(6) Å and c = 12.7000(11) Å (see details in SI Table S2, Fig. S2). FTIR spectrum of synthesized MIL-88A is presented in Fig. 2b. The first two peaks at 495 and 560 cm^{-1} were attributed to the stretching vibrations of Fe−O bonds [51]. Bending vibrations of the O-C-O group gave rise to peaks at 610 and 640 cm^{-1} [52,53]. Mode at 670 cm^{-1} was assigned to the joint contribution from torsion vibrations of C-O bonds and C═O bending [52]. The last one additionally caused a peak at 795 cm^{-1}. Two peaks at 950 and 990 cm^{-1} were attributed to the stretching of C−C bonds and bending of C−H bonds, respectively [52]. Peaks at 1120, 1160, and 1215 cm^{-1} were associated with C-O-H bending and C-O stretching vibrations. Symmetric and asymmetric vibrations of carboxyl groups gave rise to two peaks at 1390 and 1600 cm^{-1}, respectively [53]. The broad peak in the region 2750–3680 cm^{-1} is usually attributed to adsorbed water (Fig. S.3).

Fig. 3a represents TGA and DSC curves measured in the airflow for the MIL-88A sample. Three main steps could be observed during annealing. The first weight loss at 25–200 °C was designated as (1) in Fig. 3. It was attributed to the evacuation of water molecules from the pores of MIL-88A. This process is endothermic, and it corresponds to a negative peak on the DSC curve. The number of water molecules per one formula unit of MIL-88A was estimated as five according to the first weight loss (see details of TGA calculations in SI, Part 2.4, Fig. S4). The most pronounced weight loss (designated as (2) in Fig. 3a) occurred between 250 and 500 °C. It corresponds to the decomposition of MIL-88A with the production of gases from the linker counterpart and iron oxide as solid residuals (Fig. 3b). Theoretical weight loss for MIL-88A is 56%. Experimental weight loss according to TGA was very close to this value. Decomposition of MIL-88A is an exothermic process. And a positive peak was observed in the DSC curve in the temperature range of 250–500 °C. However, this peak was not smooth, as well as weight loss in this temperature range. The step in the TGA curve and the peak in the DSC curve at 250–450 °C corresponded to the formation of iron oxide with carbon shell as solid residual. Further heating led to the formation of pure iron oxide, while the carbon shell interacted with oxygen and flowed away as carbon dioxide (process (3) in Fig. 3a). Iron oxide with a carbon shell was an intermediate product in the process of MIL-88A decomposition. However, it was relatively stable, and it could indicate that the formation of carbon shells during MIL-88A annealing is a preferable process.

The chemical processes, which were observed during MIL-88A decomposition, could be represented according to the following equations:

$$Fe_3O(OH)(C_4H_2O_4)_3{\cdot}5H_2O \rightarrow Fe_3O(OH)(C_4H_2O_4)_3 + 5H_2O\uparrow \quad (1)$$

$$Fe_3O(OH)(C_4H_2O_4)_3 + 9O_2 \rightarrow 1.5Fe_2O_3 + 12CO_2\uparrow + 3.5H_2O\uparrow \quad (2)$$

$$Fe_2O_3 \cdot C + O_2 \rightarrow Fe_2O_3 + CO_2\uparrow \quad (3)$$

MIL-88A sample was composed of rod-like elongated crystals according to TEM images (Fig. 4). This shape is typical for MIL-88A material synthesized in water [54–56]. Due to highly anisotropic crystals, we measured size distribution in two separate parts. The first one was the length of crystals; it was associated with the longest axis between the two outermost points. The second one was the width of the crystals, which was perpendicular to the length. We observed that the length of crystals exhibited a relatively broad distribution of about 1–4 µm. Contrary, measured widths showed sharp distribution with an average of about 400 nm. We suppose that it could be attributed to the crystal growth process. Firstly, short diamond-like crystals are formed in the solution, while then they grow preferably in [100] direction [57].

The porosity of the MIL-88A sample is a crucial property for the successful production of composites. Fig. 5a represents nitrogen adsorption-desorption isotherms. Their shape was attributed to type I according to the IUPAC classification. This shape is typical for microporous materials. In agreement with this, the BJH method exhibited pores of about 1.1 and 1.3 nm in diameter (Fig. 5b). According to the BET model, the specific surface area was estimated as 144 m^2/g (see details in SI, Part 2.5, Table S3, Fig. S5). MIL-88A is a flexible framework that exhibits almost a reversible doubling of its cell volume while transforming from closed to open-framework topology

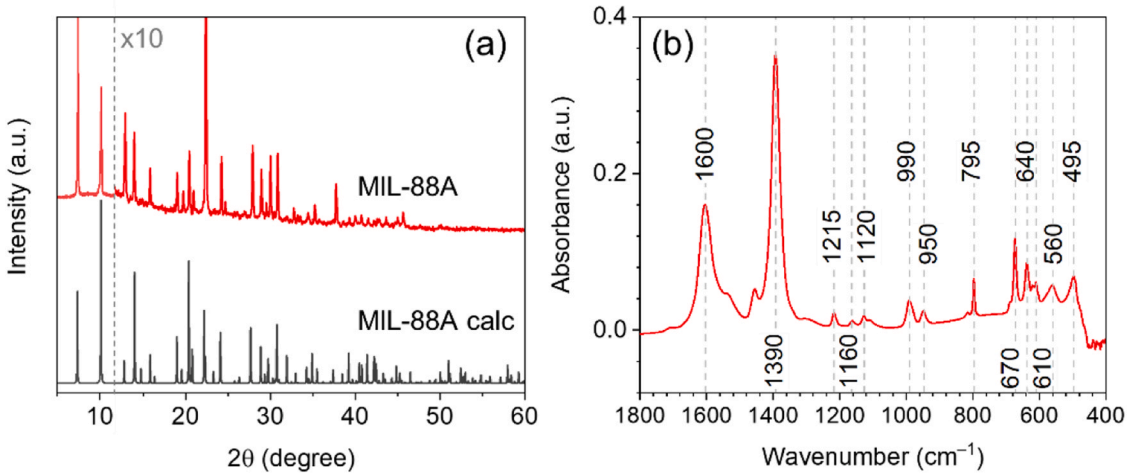

Fig. 2. (a) Powder XRD pattern of synthesized MIL-88A sample (red profile). Gray profile was calculated according to crystallographic information for "open" modification of MIL-88A [50]. After the dashed line, intensities were multiplied by 10 for better representation. (b) FTIR spectrum of MIL-88A sample in region 400–1800 cm^{-1}. Gray dashed lines represent peaks and their positions. For more details, see the text.

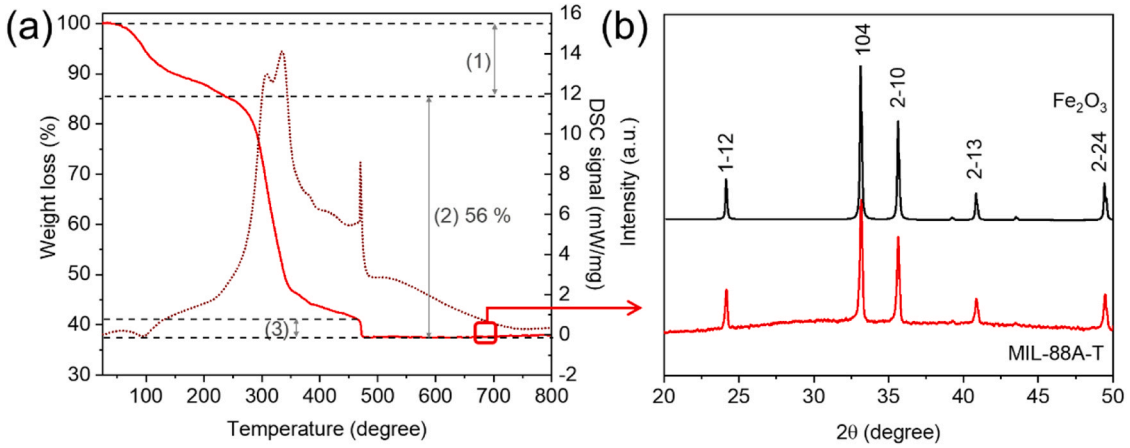

Fig. 3. (a) TGA curve (solid line) and DSC curve (dotted line) of MIL-88A sample. Processes designated as (1)–(3) are discussed in the text. (b) XRD profile of MIL-88A sample after annealing at 700 °C for 1 h (designated as MIL-88A-T). Profile Fe_2O_3 was plotted according to data for hematite from pdf-2 890596.

[50,58]. We suppose that solvent evacuation during degas treatment leads to stabilization of closed MIL-88A modification. The estimated specific surface area of the MIL-88A sample is in good agreement with reported data [59–61].

Hydrogen adsorption-desorption isotherms are provided in Fig. 5c. Hydrogen capacities for pressures 10 and 700 mmHg were 0.19 and 0.618 wt%, respectively. Fast adsorption in a low-pressure region is typical for microporous materials.

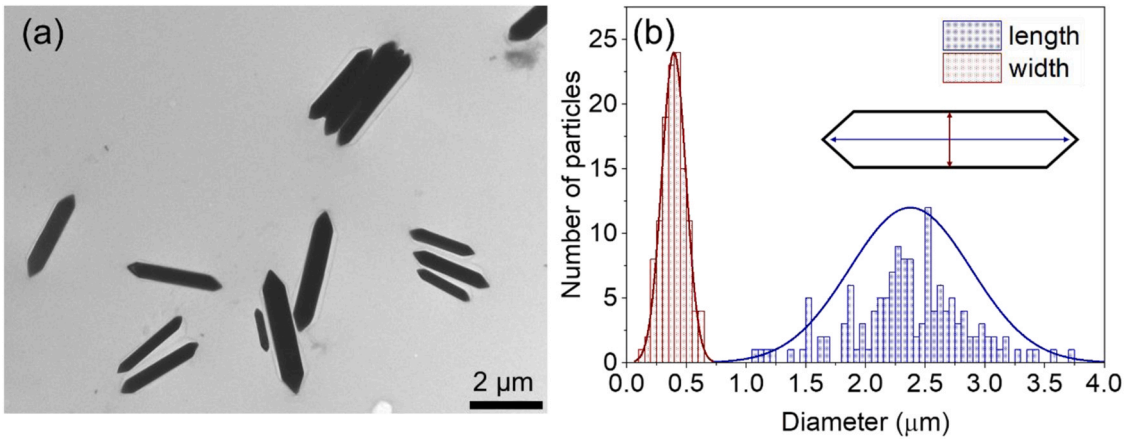

Fig. 4. (a) Representative TEM image of MIL-88A sample. (b) Particles size distribution: red bars represent the distribution of the width of crystals, while blue ones stand for the length of particles.

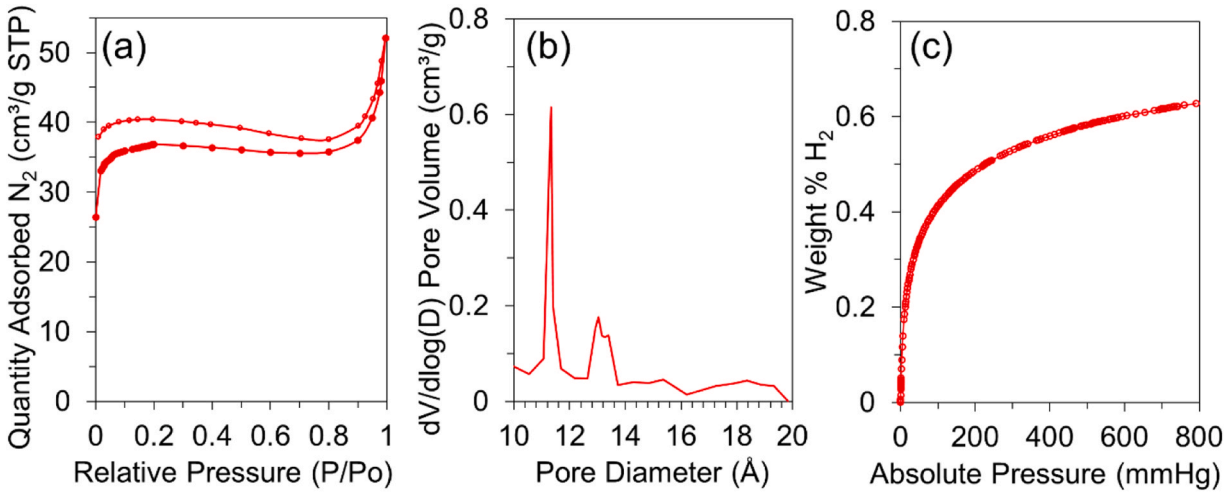

Fig. 5. (a) Nitrogen sorption isotherms of the sample MIL-88A. (b) Pore size distribution calculated according to adsorption branch of isotherm. (c) Hydrogen sorption isotherm of sample MIL-88A. Filled markers in parts (a) and (c) represent the adsorption branch of the isotherm, while empty markers designate desorption one.

2.6. FeF_2@C

The powder XRD pattern of the FeF_2@C sample is presented in Fig. 6a. All peaks were attributed to tetragonal symmetry, space group *P*42/*mnm* (136). According to XRD data, the sample was assigned to the FeF_2 phase (SI Fig. S6). Lattice constants were estimated as a = b = 4.7012(11) Å, c = 3.2968(8) Å (see details in SI Table S4, Fig. S7). XRD profile of FeF_2@C sample exhibited broad reflections due to the small size of particles. According to Sherer's equation average size of crystals was 37 nm. As reported previously, PVDF polymer under heating lost HF molecules along the polymer chain with the formation of a polygenic sequence [62,63]. Hydrofluoric acid could interact with Fe^{3+} ions in MIL-88A. Simultaneously, during the pyrolysis, linker molecules reduced iron from Fe^{3+} to Fe^{2+}. We propose the following chemical process:

$$2Fe_3O(OH)(C_4H_2O_4)_3 + 12HF \rightarrow 6FeF_2 + 13H_2O + 15CO + 9C \quad (4)$$

Fig. 6b demonstrates the Fe K-edge XAS of the MIL-88A and FeF_2@C samples. In good agreement with the proposed process (4), we observed a change in the oxidation state of iron caused by the annealing process. The spectrum of the initial MIL-88A sample fitted well with the reference Fe_2O_3 spectrum, indicating a +3 oxidation state of iron. An accurate investigation of the atomic and electronic structure of MIL-88A via the XANES method was reported previously [64]. We observed a similar position of the main peak and shoulder in the experimental MIL-88A spectrum. The pyrolysis process led to significant changes, and the spectrum of the FeF_2@C sample fitted with the $FeSO_4$ reference. It proved that synthesized FeF_2@C material contains iron +2 ions in good agreement with XRD data and the proposed reaction (4). We additionally applied Mössbauer spectroscopy to evaluate the oxidation state of iron in FeF2@C composite. According to obtained results sample contains 91% of Fe^{2+} and 9% of Fe^{3+} (Fig. S10 in SI). We suppose that the last ones were FeF_2 particles on the surface of the composite, which were oxidized by the air. However, their part is not significant. Thus, based on complex characterization, we observed a complete reduction of Fe^{3+} from MIL-88A to Fe^{2+} and good stability of obtained sample in the air atmosphere.

Sample MIL-88A-PVDF-Air was obtained in the air. According to XRD data, it was assigned to the hematite Fe_2O_3 phase (see details in SI Part 3.2, Table S4, Figs. S8, S9). Fe^{3+} ions could not be reduced in the oxidizing air medium, so they preserved the oxidation state.

The nitrogen sorption isotherm of the FeF_2@C sample is presented in Fig. 7a. Fast adsorption in a low-pressure region revealed the presence of micropores, while further nitrogen adsorption at

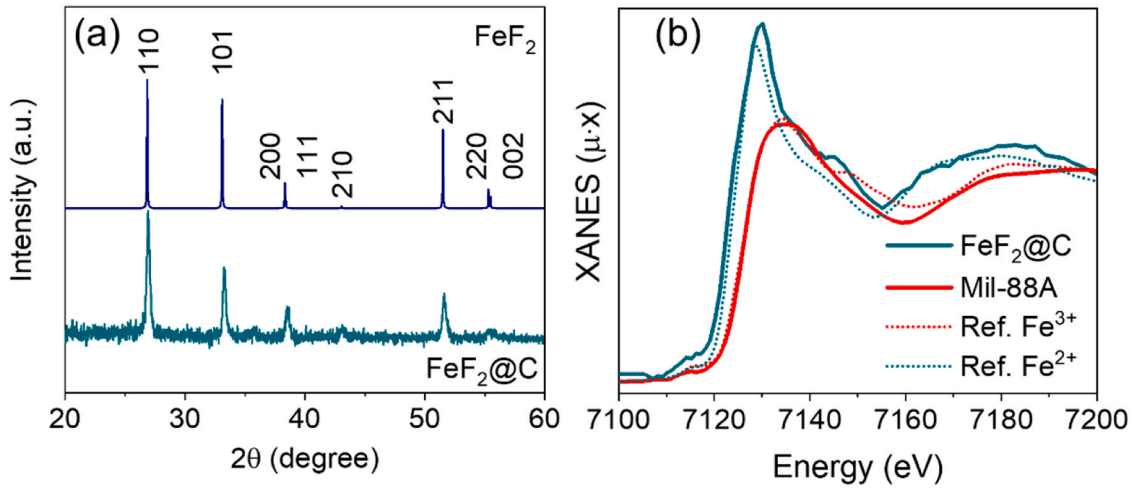

Fig. 6. (a) Powder XRD profiles of samples FeF_2@C. Profile FeF_2 was calculated according to crystallographic data from COD 9007536. (b) Fe K-edge XANES spectra for as-synthesized MIL-88A (red line) and FeF2@C (cyan line).

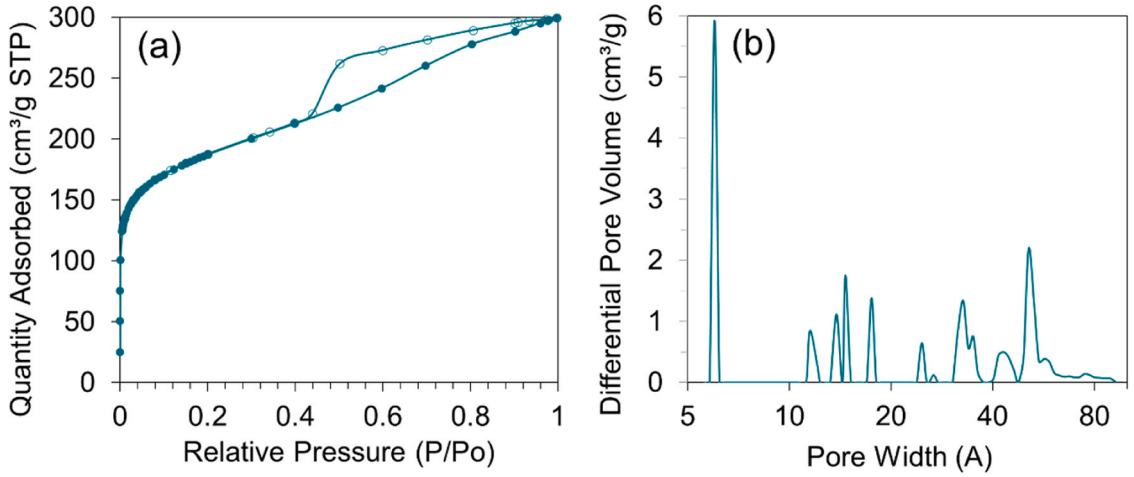

Fig. 7. (a) Nitrogen adsorption-desorption isotherms of FeF_2@C sample. Filled markers represent the adsorption branch of the isotherm, while empty markers designate desorption one. Part (b) demonstrates pore size distribution for sample FeF_2@C.

relative pressures 0.1–1.0 was attributed to the filling of meso-cavities. In agreement with the last statement, we observed a hysteresis loop at pressure region 0.4–1.0. It was associated with capillary condensation of nitrogen in mesopores. According to IUPAC notifications, the shape of hysteresis was assigned to type H4. Narrow slit-like pores are usually associated with such hysteresis. We suppose that elongated FeF_2 nanoparticles in agglomerates could form such cavities. Pores size distribution was calculated using 2D-NLDFT according to the model of finite slit pores (see inset in Fig. 7b). It showed the presence of both micropores (about 0.6 and 1–2 nm) and meso-cavities (2–8 nm). The specific surface area was estimated as 671 m^2/g according to the BET model (see details in SI Part 3.4, Table S6, Fig. S11). We suppose that the porous framework of MIL-88A after pyrolysis turned into a porous carbon shell for FeF_2 nanoparticles. Moreover, additional porous carbon was provided by PVDF molecules.

TEM image of the FeF_2@C sample is presented in Fig. 8a, b. We observed two types of particles. Most of them had an elongated shape with long rounded edges and short smoothed ends. The average width of crystals was estimated as 25 nm, while length exhibited broader distribution in the range of about 40–90 nm (Fig. 8b). Hexagonal particles were observed as an admixture to this fraction. The rod-like shape of FeF_2 crystals is referred to the tetragonal symmetry of the material [65]. We suppose that hexagonal particles represent the initial step of the crystal growth process, and further reaction results in elongated particles, which are typical for the FeF_2 phase [41,66]. Facets of nanorods are dominated by (110) direction, while smoothed ends correspond to a (001) plane. Conversion reactions occur on the surface of nanorods, and their mechanisms and rates are strongly affected by the symmetry of FeF_2 particles along with different crystallographic directions [29,67]. The process of lithium insertion within the first few atomic levels results in the disordering of FeF_2 lattice and the formation of ultrasmall Fe nanoparticles. Diffusion channels for Li-ions exist along both (110) and (001) directions [67]. According to the lower barrier along the (001) channel [67] and short-range intercalation quickly followed by conversion [29], this direction is preferable for fast Li-transport. Moreover, layer-by-layer LiF formation along the (110) direction obstructs Li^+ insertion. Thus, further lithiation proceeds in a unidirectional fashion along the length of the nanorod. Thus, minimization of the (110) surface improves both reversibility and reaction kinetics [29]. In this way, the formation of small FeF_2 nanorods with lengths less than 100 nm and hexagonal-shaped nuclei could significantly improve the electrochemical performance of the material.

FeF_2 crystals were distributed in a porous carbon matrix, and each particle was coated by a thin carbon layer (Fig. 8b). This aspect is crucial for the application of the obtained material due to pure FeF_2 is an electrical insulator. We applied electron diffraction from selected nanocrystals with both shapes (SI Fig. S12, Table S7). According to D-spacing, they were attributed to the FeF_2 phase in good agreement with powder diffraction data. EDX-mapping showed that

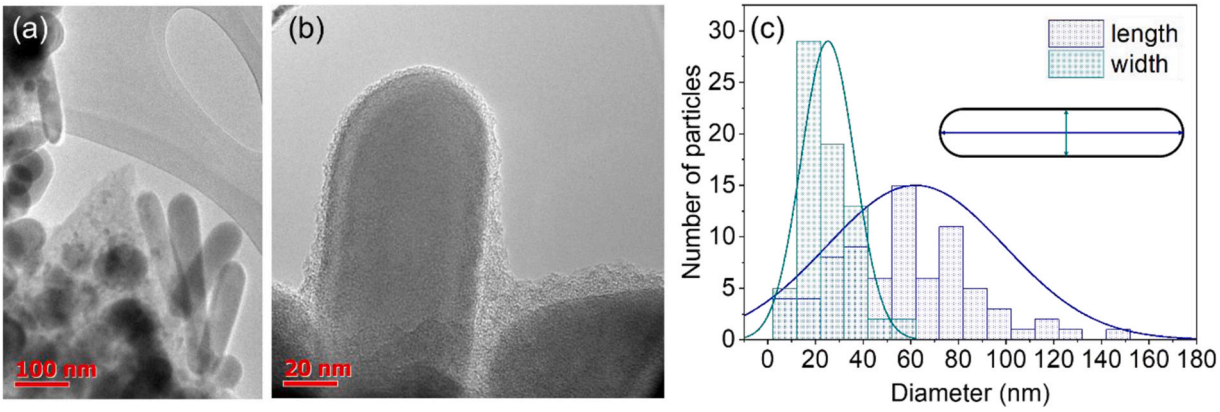

Fig. 8. (a) Representative TEM image of FeF_2@C sample. (b) Particle size distribution: cyan bars represent the distribution of the width of crystals, while dark-blue ones stand for the length of particles.

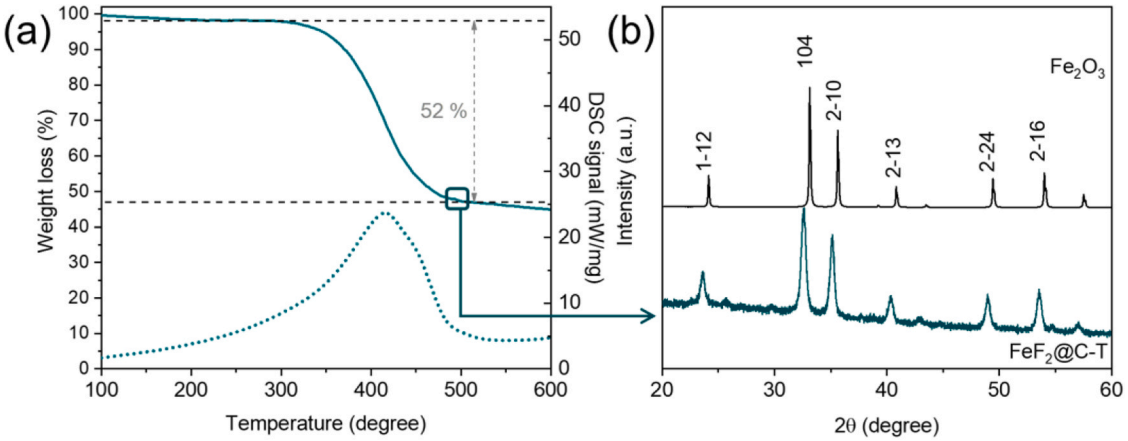

Fig. 9. (a) TGA curve (solid line) and DSC curve (dotted line) of FeF_2@C sample. (b) XRD profile of FeF_2@C sample after annealing at 500 °C for 1 h (designated as FeF_2@C-T). Profile Fe_2O_3 was plotted according to data for hematite from pdf-2 890596.

crystals were composed primarily of iron and fluoride, while porous matrix contained carbon and oxygen (SI Figs. S13, S14). The last one was associated with adsorbed water molecules due to the high porosity of carbon shells.

The amount of carbon in the FeF_2@C sample was determined according to TGA data (Fig. 9a). Annealing in the airflow resulted in the formation of Fe_2O_3 as a solid residual according to XRD (Fig. 9b). Weight loss was estimated as 52%, which corresponds to six carbon atoms per FeF_2 formula unit or 43 wt% of carbon (see details in SI Part 3.5, Fig. S16).

$$FeF_2 \cdot 6C + H_2O + 6.25O_2 \rightarrow 0.5Fe_2O_3 + 6CO_2 + 2HF \quad (5)$$

2.7. Electrochemical performance of FeF_2@carbon nanoparticles

The electrochemical performance of FeF_2@C nanoparticles was estimated by galvanostatic lithiation/de-lithiation measurements at room temperature. It was reported that the first lithiation process initiates a reduction in particle size of the reconverted FeF_2, which enhances the kinetics of the process [20]. Due to the hysteresis voltage is closely correlated to a main structural reconstitution upon a conversion reaction, it is improbable that FeF_2-LiF was involved in the main structural reconstitution through cycles after the initial charge. According to the TGA analysis, the FeF_2@C composite contains about 57% of the pure FeF_2 active phase. This results in the active phase load of 0.81 mg/cm^2 cycled with a specific current of around 300 mA/g and a current density of around 0.25 mA/cm^2. Taking into account the electrode composition and loadings, the realistic gravimetric energy density in our case is around 865 W h/kg. Fig. 10 shows the appropriately calculated values of specific capacity for galvanostatic charge-discharge in the range between 1.3 V and 4.2 V vs Li/Li$^+$ for 100 cycles. The initial discharge capacity of FeF_2 is 614 mA h/g, which is larger than the theoretical capacity (571 mA h/g) of FeF_2, likely due to the Li consumption for solid-electrolyte interface formation. However, the capacity quickly fades, roughly following a second-order exponential decay function. After 20 cycles, the capacity reaches 425 mA h/g and then continues to decrease slowly, approaching a value of 330 mA h/g during continuous cycling. One can also notice that in every cycle, the discharge capacity is higher than the charge capacity, which creates an illusion of higher than 100% efficiency. What it really means is that in every cycle on discharge, more lithium enters the material than can be extracted in the next cycle. This behavior is shown in Fig. 10 as charge/discharge efficiency calculated as a fraction of the charge capacity (amount Li extracted) relative to the discharge capacity

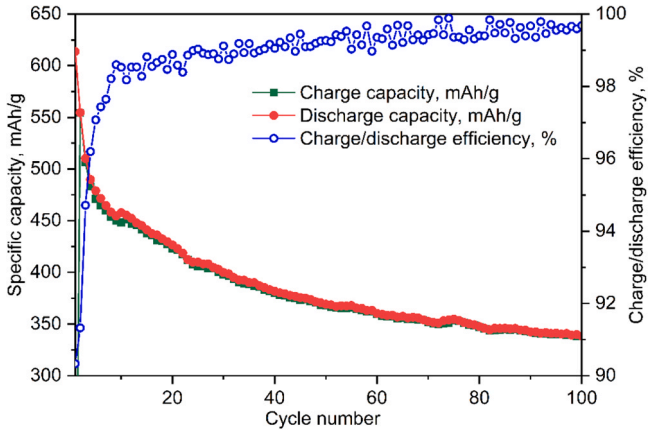

Fig. 10. Specific capacity for galvanostatic charge-discharge in the range between 1.3 V and 4.2 V vs Li/Li$^+$ for 100 cycles, calculated per mass of the pure FeF_2 active phase. Charge/discharge efficiency was calculated as a fraction of the charge capacity (amount Li extracted) relative to the discharge capacity (amount of lithium inserted) in the previous cycle.

(amount of lithium inserted) in the previous cycle. About 0.5–1% of lithium (up to 2% in the first 20 cycles and up to 10% in the first five cycles) is irreversibly trapped on the cathode side. We attribute it to unidentified side reactions. One of possible reasons might be the absorption of Li by mesoporous carbon coating or interaction with electrolyte since Fe K-edge XANES do not indicate changes in the highest achieved concentrations of Fe^0 and Fe^{2+} phases in the first discharge cycles. FeF_2@C nanoparticles show good quality and rate performance compared to other reports, especially in the FeF_2 with carbon nanotubes [21], where the obtained first discharge capacity was lower than our result of specific capacity. We assign it to a 3d-system of open pores in the carbon layer of the FeF_2@C sample.

To obtain more information about the redox occurring in the FeF_2 cell upon the second cycle, ex-situ XAS studied both an electronic environmental and local iron structure. Fig. 11 shows the Fe K-edge X-ray absorption spectra obtained during the full 2nd cycle of a charge and discharge spectra measured for the lowest (1.3 V) and highest (4.1 V) cell potential correspondingly. The chemical shift of the edge position indicates the change in the oxidation state of iron. The pre-edge and main edge of the FeF_2 electrode are closed to those of Fe^{2+} (reference $FeSO_4$) and Fe^0 (reference Fe-metal). Upon charge up to 1.3 V appearance shoulder at the pre-edge, we noted that iron had a mixed oxidation state – Fe^0 (metallic) and Fe^{+2}. After the discharge, that shoulder disappeared, and the spectra of the Fe K-

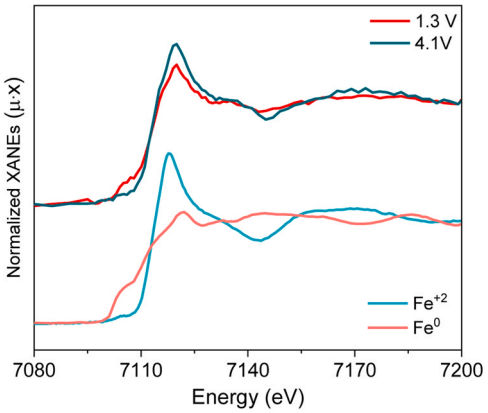

Fig. 11. Selected Ex-situ XANES spectra upon the 2nd cycle of Fe K-edge along with respected references.

edge returned to their initial position, demonstrating a sharp pre-edge and main edge corresponding to the Fe^{+2} oxidation state. So the electrochemical process could be represented according to the following equation:

$$FeF_2 + 2Li^+ + 2\acute{e} \rightarrow Fe + 2LiF \quad (6)$$

3. Conclusions

In the present work, we propose a simple and scalable method of FeF_2 cathode production. We used the metal-organic framework MIL-88A as a precursor. It was obtained in a water medium from $FeCl_3$ and fumaric acid. MIL-88A was considered as a source of both Fe^{3+} ions and carbon during subsequent pyrolysis. Moreover, we used the porous structure of this material as a host for PVDF molecules. For this aim, we mixed as-prepared MIL-88A with PVDF in methanol. Pyrolysis of this reaction mixture resulted in simultaneous interaction of iron ions with fluoride and reduction of Fe^{3+} to Fe^{2+}. PVDF molecules and organic counterparts of MIL-88A after pyrolysis transformed into microporous conductive carbon containers for FeF_2 nanoparticles. The obtained composite material was tested as a cathode for LIB. It exhibited good stability and high capacity. By applying the Ex-situ XANES measurements, the metallic phase of iron appears during the charge due to a shoulder in the pre-edge. After discharge, the spectrum returns to the initial phase with a sharp main peak and pre-edge, indicating a +2 oxidation state of iron.

CRediT authorship contribution statement

Vera V. Butova: Conceptualization, Data curation, Writing – original draft. **Abdelaziz M. Aboraia**: Validation, Formal analysis. **Victor V. Shapovalov:** Formal analysis, Writing – review & editing. **Narek A. Dzhangiryan***:* Validation, Formal analysis, **Elizaveta D. Papkovskaya:** Validation, Formal analysis. **Oleg I. Ilin**: Methodology, Investigation. **Stanislav P. Kubrin**: Formal analysis. **Alexander A. Guda**: Investigation, Writing – review & editing. **Alexander V. Soldatov**: Supervision, Resources.

Declaration of Competing Interest

The authors declare that they have no known competing financial interests or personal relationships that could have appeared to influence the work reported in this paper.

Acknowledgements

The research was financially supported by the Ministry of Science and Higher Education of the Russian Federation (No. 0852-2020-0019).

Appendix A. Supporting information

Supplementary data associated with this article can be found in the online version at doi:10.1016/j.jallcom.2022.165438.

References

[1] J. Cabana, L. Monconduit, D. Larcher, M.R. Palacin, Beyond intercalation-based Li-ion batteries: the state of the art and challenges of electrode materials reacting through conversion reactions, Adv. Mater. 22 (35) (2010) E170–E192.
[2] N. Nitta, F.X. Wu, J.T. Lee, G. Yushin, Li-ion battery materials: present and future, Mater. Today 18 (5) (2015) 252–264.
[3] G.K. Zhong, K. Qu, C.L. Ren, Y. Su, B. Fu, M.F. Zi, L.Y.F. Dai, Q. Xiao, J. Xu, X.L. Zhong, F. An, M. Ye, S.M. Ke, S.H. Xie, J.B. Wang, P. Gao, J.Y. Li, Epitaxial array of Fe3O4 nanodots for high rate high capacity conversion type lithium ion batteries electrode with long cycling life, Nano Energy (2020) 74.
[4] L.M. Housel, A. Abraham, G.D. Renderos, K.J. Takeuchi, E.S. Takeuchi, A.C. Marschilok, Surface electrolyte interphase control on magnetite, Fe3O4, electrodes: impact on electrochemistry, Mrs Adv. 3 (11) (2018) 581–586.
[5] N.X. Zhu, J.P. Liu, S.K. Zhang, L. Zhang, X.J. Liu, D. Wang, Y.H. Chen, Peapod-like architectures with CuO microspheres encapsulated within MXene as a conversion electrode for lithium-ion batteries, Chem. Commun. 58 (8) (2022) 1195–1198.
[6] Z. Qian, H.N. Zhang, G.Z. Jiang, Y.W. Bai, Y.Y. Ren, W.Z. Du, R. Ahuja, Ab initio screening of doped Mg(AlH4)(2) systems for conversion-type lithium storage, Materials 12 (2019) 16.
[7] L. Huang, L. Aymard, J.P. Bonnet, MgH2-TiH2 mixture as an anode for lithium-ion batteries: synergic enhancement of the conversion electrode electrochemical performance, J. Mater. Chem. A 3 (29) (2015) 15091–15096.
[8] Z. Qian, G.Z. Jiang, Y.Y. Ren, X. Nie, R. Ahuja, Atomistic modeling of various doped Mg2NiH4 as conversion electrode materials for lithium storage, Crystals 9 (2019) 5.
[9] D.M. Halat, S. Britto, K.J. Griffith, E. Jonsson, C.P. Grey, Natural abundance solid-state S-33 NMR study of NbS3: applications for battery conversion electrodes, Chem. Commun. 55 (84) (2019) 12687–12690.
[10] H.W. Tao, M. Zhou, R.X. Wang, K.L. Wang, S.J. Cheng, K. Jiang, TiS2 as an advanced conversion electrode for sodium-ion batteries with ultra-high capacity and long-cycle life, Adv. Sci. 5 (2018) 11.
[11] X.J. Li, A.L. Hector, J.R. Owen, Evaluation of Cu3N and CuO as negative electrode materials for sodium batteries, J. Phys. Chem. C 118 (51) (2014) 29568–29573.
[12] L. Baggetto, N.A.M. Verhaegh, R.A.H. Niessen, F. Roozeboom, J.C. Jumas, P.H.L. Notten, Tin nitride thin films as negative electrode material for lithium-ion solid-state batteries, J. Electrochem. Soc. 157 (3) (2010) A340–A347.
[13] B. Milke, C. Wall, S. Metzke, G. Clavel, M. Fichtner, C. Giordano, A simple synthesis of MnN0.43@C nanocomposite: characterization and application as battery material, J. Nanopart. Res. 16 (2014) 12.
[14] W. Tong, G.G. Amatucci, Silver copper fluoride: a novel perovskite cathode for lithium batteries, J. Power Sources 362 (2017) 86–91.
[15] D.H. Lee, K. Carroll, S. Calvin, K. Chapman, P. Chupas, Y.S. Meng, Understanding improved electrochemical properties in nickel fluoride conversion electrode materials by X-ray absorption spectroscopy and pair distribution function, Abstr. Pap. Am. Chem. Soc. (2013) 245.
[16] F. Badway, F. Cosandey, N. Pereira, G.G. Amatucci, Carbon metal fluoride nanocomposites – high-capacity reversible metal fluoride conversion materials as rechargeable positive electrodes for Li batteries, J. Electrochem. Soc. 150 (10) (2003) A1318–A1327.
[17] F. Badway, N. Pereira, F. Cosandey, G.G. Amatucci, Carbon-metal fluoride nanocomposites: structure and electrochemistry of FeF_3:C, J. Electrochem. Soc. 150 (9) (2003) A1209.
[18] C. Li, L. Gu, S. Tsukimoto, P.A. Van Aken, J. Maier, Low-temperature ionic-liquid-based synthesis of nanostructured iron-based fluoride cathodes for lithium batteries, Adv. Mater. 22 (33) (2010) 3650–3654.
[19] I. Plitz, F. Badway, J. Al-Sharab, A. DuPasquier, F. Cosandey, G.G. Amatucci, Structure and electrochemistry of carbon-metal fluoride nanocomposites fabricated by solid-state redox conversion reaction, J. Electrochem. Soc. 152 (2) (2004) A307.
[20] F. Wang, R. Robert, N.A. Chernova, N. Pereira, F. Omenya, F. Badway, X. Hua, M. Ruotolo, R. Zhang, L. Wu, Conversion reaction mechanisms in lithium ion batteries: study of the binary metal fluoride electrodes, J. Am. Chem. Soc. 133 (46) (2011) 18828–18836.
[21] J. Zhou, D. Zhang, X. Zhang, H. Song, X. Chen, Carbon-nanotube-encapsulated FeF2 nanorods for high-performance lithium-ion cathode materials, ACS Appl. Mater. Interfaces 6 (23) (2014) 21223–21229.
[22] F. Wang, H.C. Yu, M.H. Chen, L.J. Wu, N. Pereira, K. Thornton, A. Van der Ven, Y.M. Zhu, G.G. Amatucci, J. Graetz, Tracking lithium transport and electrochemical reactions in nanoparticles, Nat. Commun. 3 (2012) 8.

[23] D.E. Conte, N. Pinna, A review on the application of iron (III) fluorides as positive electrodes for secondary cells, Mater. Renew. Sustain. Energy 3 (4) (2014) 1–22.
[24] M.A. Reddy, B. Breitung, V.S.K. Chakravadhanula, M. Helen, R. Witte, C. Rongeat, C. Kübel, H. Hahn, M. Fichtner, Facile synthesis of C–FeF2 nanocomposites from CFx: influence of carbon precursor on reversible lithium storage, RSC Adv. 8 (64) (2018) 36802–36811.
[25] H. Liang, Z. Hu, Z. Zhao, D. Chen, H. Zhang, H. Wang, X. Wang, Q. Li, X. Guo, H. Li, Dendrite-structured FeF2 consisting of closely linked nanoparticles as cathode for high-performance lithium-ion capacitors, J. Energy Chem. 55 (2021) 517–523.
[26] W. Gu, A. Magasinski, B. Zdyrko, G. Yushin, Metal fluorides nanoconfined in carbon nanopores as reversible high capacity cathodes for Li and Li-ion rechargeable batteries: FeF2 as an example, Adv. Energy Mater. 5 (4) (2015) 1401148.
[27] Q. Huang, T.P. Pollard, X. Ren, D. Kim, A. Magasinski, O. Borodin, G. Yushin, Fading mechanisms and voltage hysteresis in FeF2–NiF2 solid solution cathodes for lithium and lithium-ion batteries, Small 15 (6) (2019) 1804670.
[28] Y.L. Zhang, L. Wang, J.J. Li, L. Wen, X.M. He, A one-pot approach towards FeF2-carbon core-shell composite and its application in lithium ion batteries, J. Alloy. Compd. 606 (2014) 226–230.
[29] A.B.W. Xiao, H.J. Lee, I. Capone, A. Robertson, T.U. Wi, J. Fawdon, S. Wheeler, H.W. Lee, N. Grobert, M. Pasta, Understanding the conversion mechanism and performance of monodisperse FeF2 nanocrystal cathodes, Nat. Mater. 19 (6) (2020) 644.
[30] Q. Huang, K. Turcheniuk, X. Ren, A. Magasinski, A.-Y. Song, Y. Xiao, D. Kim, G. Yushin, Cycle stability of conversion-type iron fluoride lithium battery cathode at elevated temperatures in polymer electrolyte composites, Nat. Mater. 18 (12) (2019) 1343–1349.
[31] M. Helen, M. Fichtner, M.A. Reddy, Electrochemical synthesis of carbon-metal fluoride nanocomposites as cathode materials for lithium batteries, Electrochem. Commun. 120 (2020) 6.
[32] A.Y. Maulana, C.M. Futalan, J. Kim, MOF-derived FeF2 nanoparticles@graphitic carbon undergoing in situ phase transformation to FeF3 as a superior sodium-ion cathode material, J. Alloy. Compd. (2020) *840*.
[33] D.J. Tranchemontagne, J.L. Mendoza-Cortes, M. O'Keeffe, O.M. Yaghi, Secondary building units, nets and bonding in the chemistry of metal-organic frameworks, Chem. Soc. Rev. 38 (5) (2009) 1257–1283.
[34] V.V. Butova, M.A. Soldatov, A.A. Guda, K.A. Lomachenko, C. Lamberti, Metal-organic frameworks: structure, properties, methods of synthesis and characterization, Russ. Chem. Rev. 85 (3) (2016) 280–307.
[35] W. Xia, A. Mahmood, R.Q. Zou, Q. Xu, Metal-organic frameworks and their derived nanostructures for electrochemical energy storage and conversion, Energy Environ. Sci. 8 (7) (2015) 1837–1866.
[36] R.R. Salunkhe, Y.V. Kaneti, Y. Yamauchi, Metal-organic framework-derived nanoporous metal oxides toward supercapacitor applications: progress and prospects, ACS Nano 11 (6) (2017) 5293–5308.
[37] V.V. Butova, V.A. Polyakov, E.A. Erofeeva, S.A. Efimova, M.A. Soldatov, A.L. Trigub, Y.V. Rusalev, A.V. Soldatov, Synthesis of ZnO nanoparticles doped with cobalt using bimetallic ZIFs as sacrificial agents, Nanomaterials 10 (7) (2020) 13.
[38] V.V. Butova, V.A. Polyakov, E.A. Erofeeva, Z.Y. Li, M.A. Soldatov, A.V. Soldatov, Synthesis of zinc oxide nanoparticles coated with silicon oxide, Dokl. Chem. 492 (1) (2020) 69–72.
[39] Y.J. Cao, W. Yang, M.Y. Wang, N. Wu, L.W. Zhang, Q.X. Guan, H. Guo, Metal-organic frameworks as highly efficient electrodes for long cycling stability supercapacitors, Int. J. Hydrog. Energy 46 (35) (2021) 18179–18206.
[40] M.A. Yanuar, J. Kim, FeOF nanoparticles wrapped by graphitic carbon layers prepared from Fe-MIL-88B as a cathode material for sodium-ion batteries, Carbon 149 (2019) 483–491.
[41] Q.X. Cheng, Y.Y. Pan, Y.Y. Chen, A. Zeb, X.M. Lin, Z.Z. Yuan, J.C. Liu, Nanostructured iron fluoride derived from fe-based metal-organic framework for lithium ion battery cathodes, Inorg. Chem. 59 (17) (2020) 12700–12710.
[42] C. Serre, C. Mellot-Draznieks, S. Surblé, N. Audebrand, Y. Filinchuk, G. Férey, Role of solvent-host interactions that lead to very large swelling of hybrid frameworks, Science 315 (5820) (2007) 1828–1831.
[43] T. Chalati, P. Horcajada, R. Gref, P. Couvreur, C. Serre, Optimisation of the synthesis of MOF nanoparticles made of flexible porous iron fumarate MIL-88A, J. Mater. Chem. 21 (7) (2011) 2220–2227.
[44] L. Wang, Y.Y. Zhang, X. Li, Y.Z. Xie, J. He, J. Yu, Y.H. Song, The MIL-88A-derived Fe3O4-carbon hierarchical nanocomposites for electrochemical sensing, Sci. Rep. 5 (2015) 12.
[45] L. Wang, J. Yu, X.T. Dong, X. Li, Y.Z. Xie, S.H. Chen, P. Li, H.Q. Hou, Y.H. Song, Three-Dimensional macroporous carbon/Fe3O4-doped porous carbon nanorods for high-performance supercapacitor, ACS Sustain. Chem. Eng. 4 (3) (2016) 1531–1537.
[46] Y. Wang, X.M. Guo, Z.K. Wang, M.F. Lu, B. Wu, Y. Wang, C. Yan, A.H. Yuan, H.X. Yang, Controlled pyrolysis of MIL-88A to Fe2O3@C nanocomposites with varied morphologies and phases for advanced lithium storage, J. Mater. Chem. A 5 (48) (2017) 25562–25573.
[47] Z.K. Wang, Z.R. Zhang, J. Xia, W. Wang, S.S. Sun, L. Liu, H.X. Yang, Fe2O3@C core@shell nanotubes: porous Fe2O3 nanotubes derived from MIL-88A as cores and carbon as shells for high power lithium ion batteries, J. Alloy. Compd. 769 (2018) 969–976.
[48] V. Petříček, M. Dušek, L. Palatinus, Crystallographic computing system JANA2006: general features, Z. Krist. 229 (5) (2014) 345–352.
[49] B. Ravel, M. Newville, ATHENA, ARTEMIS, HEPHAESTUS: data analysis for X-ray absorption spectroscopy using IFEFFIT, J. Synchrotron Radiat. 12 (4) (2005) 537–541.
[50] C. Serre, C. Mellot-Draznieks, S. Surble, N. Audebrand, Y. Filinchuk, G. Ferey, Role of solvent-host interactions that lead to very large swelling of hybrid frameworks, Science 315 (5820) (2007) 1828–1831.
[51] T. Zhang, N. Zhao, J. Li, H. Gong, T. An, F. Zhao, H. Ma, Thermal behavior of nitrocellulose-based superthermites: effects of nano-Fe2O3 with three morphologies, RSC Adv. 7 (38) (2017) 23583–23590.
[52] E.M.S. Maçôas, R. Fausto, J. Lundell, M. Pettersson, L. Khriachtchev, M. Räsänen, A matrix isolation spectroscopic and quantum chemical study of fumaric and maleic acid, J. Phys. Chem. A 105 (15) (2001) 3922–3933.
[53] K.Y.A. Lin, H.A. Chang, C.J. Hsu, Iron-based metal organic framework, MIL-88A, as a heterogeneous persulfate catalyst for decolorization of Rhodamine B in water, RSC Adv. 5 (41) (2015) 32520–32530.
[54] S.G. Khasevani, M.R. Gholami, Novel MIL-88A/g-C3N4 nanocomposites: fabrication, characterization and it application as a photocatalyst, Inorg. Chem. Commun. 102 (2019) 221–228.
[55] Z.W. Shao, D.F. Zhang, H. Li, C.H. Su, X.P. Pu, Y.L. Geng, Fabrication of MIL-88A/g-C3N4 direct Z-scheme heterojunction with enhanced visible-light photocatalytic activity, Sep. Purif. Technol. 220 (2019) 16–24.
[56] Y. Zhang, J.B. Zhou, X. Chen, L. Wang, W.Q. Cai, Coupling of heterogeneous advanced oxidation processes and photocatalysis in efficient degradation of tetracycline hydrochloride by Fe-based MOFs: synergistic effect and degradation pathway, Chem. Eng. J. 369 (2019) 745–757.
[57] X.Y. Liao, F. Wang, F. Wang, Y. Cai, Y. Yao, B.T. Teng, Q.L. Hao, S.X. Lu, Synthesis of (100) surface oriented MIL-88A-Fe with rod-like structure and its enhanced fenton-like performance for phenol removal, Appl. Catal. B-Environ. 259 (2019) 11.
[58] C. Mellot-Draznieks, C. Serre, S. Surble, N. Audebrand, G. Ferey, Very large swelling in hybrid frameworks: a combined computational and powder diffraction study, J. Am. Chem. Soc. 127 (46) (2005) 16273–16278.
[59] J. Amaro-Gahete, R. Klee, D. Esquivel, J.R. Ruiz, C. Jimenez-Sanchidrian, F.J. Romero-Salguero, Fast ultrasound-assisted synthesis of highly crystalline MIL-88A particles and their application as ethylene adsorbents, Ultrason. Sonochem. 50 (2019) 59–66.
[60] W.Y. Huang, C.W. Jing, X.D. Zhang, M.Q. Tang, L. Tang, M.H. Wu, N. Liu, Integration of plasmonic effect into spindle-shaped MIL-88A(Fe): steering charge flow for enhanced visible-light photocatalytic degradation of ibuprofen, Chem. Eng. J. 349 (2018) 603–612.
[61] X.Y. Liao, F. Wang, F. Wang, Y. Cai, Y. Yao, B.T. Teng, Q.L. Hao, S.X. Lu, Synthesis of (100) surface oriented MIL-88A-Fe with rod-like structure and its enhanced fenton-like performance for phenol removal, Appl. Catal. B-Environ. (2019) *259*.
[62] G. Botelho, S. Lanceros-Mendez, A.M. Gonçalves, V. Sencadas, J.G. Rocha, Relationship between processing conditions, defects and thermal degradation of poly(vinylidene fluoride) in the β-phase, J. Non-Cryst. Solids 354 (1) (2008) 72–78.
[63] A.J. de Jesus Silva, M.M. Contreras, C.R. Nascimento, M.F. da Costa, Kinetics of thermal degradation and lifetime study of poly(vinylidene fluoride) (PVDF) subjected to bioethanol fuel accelerated aging, Heliyon 6 (7) (2020) e04573.
[64] P.V. Medvedev, M.A. Soldatov, V.V. Shapovalov, A.A. Tereshchenko, I.E. Gorban, A.G. Fedorenko, A.V. Soldatov, Analysis of the local atomic structure of the MIL-88a metal-organic framework by computer simulation using XANES data, Jetp Lett. 108 (5) (2018) 318–325.
[65] K. Karki, L.J. Wu, Y. Ma, M.J. Armstrong, J.D. Holmes, S.H. Garofalini, Y.M. Zhu, E.A. Stach, F. Wang, Revisiting conversion reaction mechanisms in lithium batteries: lithiation-driven topotactic transformation in FeF2, J. Am. Chem. Soc. 140 (51) (2018) 17915–17922.
[66] Y. Zhang, L. Wang, J. Li, L. Wen, X. He, A one-pot approach towards FeF2–carbon core–shell composite and its application in lithium ion batteries, J. Alloy. Compd. 606 (2014) 226–230.
[67] Y. Ma, S.H. Garofalini, Atomistic insights into the conversion reaction in iron fluoride: a dynamically adaptive force field approach, J. Am. Chem. Soc. 134 (19) (2012) 8205–8211.